Topographic-pattern-induced homeotropic alignment of liquid crystals

Youngwoo Yi,[1] Giuseppe Lombardo,[2] Neil Ashby,[3] Riccardo Barberi,[2] Joseph E. Maclennan,[1] and Noel A. Clark[1,*]
[1]*Department of Physics and Liquid Crystal Materials Research Center, University of Colorado, Boulder, Colorado 80309-0390, USA*
[2]*Department of Physics, CNR-INFM LiCryL, Cemif.Cal, University of Calabria, 87036 Rende, Italy*
[3]*Department of Physics, University of Colorado, Boulder, Colorado 80309-0390, USA*
(Received 14 November 2008; published 9 April 2009)

Polymer films nanoimprinted with checkerboard patterns of square wells align calamitic (rodlike) liquid crystals vertically, horizontally, or tilted depending on the depth/width ratio of the wells. The liquid crystal prefers planar orientation on polymer films that are smooth but when the films are topographically patterned, the increasing elastic energy density as the wells become narrower eventually overcomes the surface anchoring of the polymer and the liquid crystal director field makes a transition from planar to homeotropic. Similar effects have been demonstrated in both nematics and smectics, and the behavior is confirmed by theory and computer simulation.

DOI: 10.1103/PhysRevE.79.041701 PACS number(s): 61.30.Hn, 61.30.Gd, 61.30.Dk, 81.65.Cf

I. INTRODUCTION

Controlling the alignment of anisotropic soft matter using engineered surfaces is of great interest as a fundamental problem as well as in applications such as liquid crystal (LC) devices and organic electronics and photonics [1–5]. Topographic patterning has been used with some success to align a variety of soft materials by guiding their self-assembly on prepared substrates [6–15], the scale, and geometry of the patterns being tailored to achieve specific alignment conditions. Most previous studies of the guided alignment of LCs have been limited to surface modifications producing in-plane (planar) alignment [8–13]. Obtaining vertical (homeotropic) or tilted molecular alignment is crucial, however, for organic photonics as well as for advanced LC displays [1,2,14–17]. We show here that calamitic (rod-shaped) LCs which have planar alignment on a smooth polymer film adopt tilted or homeotropic (vertical) alignment when this film is imprinted with periodic patterns of nanoindentations that are sufficiently narrow and deep.

Uniform alignment of liquid crystals, a necessary condition in most LC applications, is commonly achieved by mechanical rubbing, a technique best suited to achieving uniform planar alignment of LCs over large areas. More sophisticated and versatile alignment schemes are necessary to expand the possible applications of LCs. With this goal, many alternative techniques including photoalignment and alignment by chemically patterned surfaces have been explored [18–21]. We have studied the alignment of LCs by topographic patterning, an alignment technique, which is particularly interesting because the three-dimensional (3D) shape and scale of the patterns can potentially be engineered to control the organization and, in principle, the local order of a variety of LCs, with different molecular shapes and exhibiting different phases. This method exploits the well-known tendency of LCs to minimize their elastic and anchoring energy in the vicinity of a topographically patterned substrate in order to manipulate locally the overall alignment of the LC molecules in cells that are several microns thick [6,7]. For example, sixfold and fourfold symmetric patterns have been demonstrated to give in-plane multistable alignment of the director, and topographic line patterns have been used for zenithal bistable alignment, which exploits switching between vertical and hybrid alignments, raising the prospect of novel displays with ultralow power consumption [3,8,9,17].

The direct fabrication of nanoscale topographically patterned devices is costly and time consuming because this generally involves electron-beam (e-beam) lithography or atomic force microscopy (AFM), where patterns are written point by point or inscribed line by line on each individual substrate. Using nanoimprinting techniques, however, allows many replicas to be produced from a master mold [22,23]. In this process, plastic photopolymerizable material is spin coated onto a substrate, squeezed tight against the mold, and then polymerized *in situ* by UV light. The substrate with the now topographically patterned polymerized surface (the "replica") is then separated from the mold. Both uniform and bistable in-plane alignment of nematics by such nanoimprinted polymer films have been observed [9–13].

The size of the nanoimprinted patterns depends on the mold fabrication technique. Nanoscale molds are conventionally prepared by e-beam lithography or UV photolithography, where the pattern size is usually on the order of 0.1–1 mm. By stitching the patterns together in e-beam writing, the pattern size of the molds can be increased to about ~1 cm [24]. Although this size is not large enough for regular displays, nanoimprinting is nevertheless a convenient tool to study self-assembly of LCs on 3D patterns of various geometry and scales, with potential application to advanced small scale displays, nanophotonics, or electro-optics.

Homeotropic alignment in nematic LC cells has traditionally been obtained using special polyimide films, photopolymers, or hydrophobic self-assembled monolayers (SAMs) [25–28]. There have also been a few investigations of using structured surfaces to induce nonplanar alignment of the director. For example, Lazarouk *et al.* [29] recently demonstrated that porous anodic nanostructures give homeotropic alignment and Zhang *et al.* [14] reported a transition of the tilt angle (the angle between the surface and the director)

*noel.clark@colorado.edu

from planar to a ~40° pretilt of a nematic LC on polymer films linearly patterned in alternating directions using AFM oxidation. Kitson and Geisow [15] used micron-scale arrays of square posts prepared by photolithography to control the tilt of the LC director from the surface and to achieve bistability.

In this paper, we describe the alignment of calamitic LCs by three-dimensional checkerboard patterns made using thiol-ene photopolymerization-based nanoimprinting. By reducing the periodicity of the patterns, we can achieve uniform homeotropic alignment of both nematics and semetics. Homeotropic alignment induced by topographic patterning has not been observed previously, possibly due to the strict requirements on the dimensions of the patterns required, as will become apparent below.

II. EXPERIMENT

A. Mold preparation

The mold was prepared using electron-beam lithography and successive reactive ion etching (RIE). A superpolished silica wafer (size: 12.5 mm; thickness: 3.2 mm) was cleaned with acetone and methanol and then coated with 10 nm of chromium by electron-beam evaporation. The wafer was then coated with poly(methyl methacrylate) (PMMA), with spin coating at 4000 rpm for 40 s. The coated wafer was then baked on a hotplate at 180 °C for 5 min. Patterns of checkerboards were written on the PMMA using an electron-beam writing system, JEOL 6400 SEM controlled by NanoPattern Generation System (JC Nabity). Regions about 80 μm × 80 μm in size were written with exposure doses of 260 μC/cm^2. The sizes of the squares in the three different patterned regions were 200, 400, and 600 nm, respectively. The PMMA film was developed in a solution (MIBK and IPA, 1:3 by volume) for 60 s and rinsed in another solution (MIBK and IPA, 1:9 by volume) for 20 s. The wafer was baked again on a hot plate at 100 °C for 3 min. The exposed chromium film was removed by wet etching, and then the silica plate was etched 420 nm into the substrate with the chromium pattern as an etch resist using a RIE system. The RIE process was carried out in octafluorocyclobutane (C_4F_8) plasma in an inductively coupled plasma etching system (MESC Multiplex ICP) with a chamber pressure of 6.6 mTorr. The chromium coating was then removed by wet etching. Finally, an *n*-octadecyltrichlorosilane (OTS) self-assembled monolayer was coated on the patterned silica wafer to reduce the surface free energy of the mold.

B. Nanoimprinting

Replicas of the mold were made by a nanoimprint process using photopolymerization [22]. A small amount of the thiol-ene photopolymerizable material was put on a small glass slide (~10 mm × 10 mm), which was then pressed against the mold at about 20 psi in a nitrogen gas chamber and exposed to UV light (λ=365 nm) from light emitting diodes for 5 min to polymerize the material under pressure. The slide was then separated from the mold, leaving a replica of the mold on the surface of the polymer film. The polymerizable material is a mixture of triallyl-1,3,5-triazine-2,4,6(1H,3H,5H)-trione and pentaerythritol tetrakis(3-mercaptopropionate) with the addition of 0.1 wt % photoinitiator [2,2-dimethoxy-2-phenylacetophenone (DMPA)] [30,31].

C. Measurement of anchoring energy

The anchoring energy of a smooth thiol-ene polymer film was determined by measuring the optical transmission of a homogeneous nematic cell as a function of applied voltage across the cell using a 5 kHz square wave. The cell was prepared using two polymer replicas with line patterns 8 μm wide and ~400 nm high prepared on ITO-coated glass slides. The thickness of the polymer films (3.1 and 3.8 μm) was found by measuring the interference of light before separating each replica from the mold. The slides were positioned such that the patterns on opposite cell surfaces were parallel and overlapping. The empty cell gap was measured to be 3.8 μm by interference spectroscopy. After filling with nematic LC (5CB), the cell showed uniform alignment.

The light from a halogen lamp passed through a polarizer, the cell, and then an analyzer to a spectrometer. The polarizer and analyzer were crossed and oriented at 45° to the line pattern. The optical transmission T was measured at 458 nm, the wavelength at which the transmission was a maximum with no voltage applied across the cell, as a function of the applied electric field. The retardation Γ was computed from the transmission using the relation, $T \approx \sin^2(\Gamma/2)$. The retardation at 0 V was found to be 9.4 rad, which matches the retardation $\Gamma = (2\pi\Delta nd/\lambda)$ calculated assuming the director is nearly parallel to the polymer surface, confirming that the polymer favors planar orientation. The voltage at which the retardation went to zero was 170 V, from which the saturation voltage V_s across the 5CB layer, assumed to have a dielectric constant of $\varepsilon_{LC}=18$, was calculated to be 22.6 V. The dielectric constant of the polymer ($\varepsilon_P=5$) was found by measuring the capacitance of a capacitor filled with a polymer film of known thickness. Finally, the anchoring energy γ of the polymer film was calculated to be 9×10^{-5} J m^{-2} = 0.09 erg cm^{-2} using the following relation:

$$\gamma = \frac{V_s K_2 (\varepsilon_0 \Delta\varepsilon K_3)^{1/2}}{tK_1},$$

where K_1, K_2, and K_3 are the splay, twist, and bend Frank elastic constants of 5CB, $\Delta\varepsilon$ is the dielectric anisotropy of 5CB, and ε_0 is the permittivity of free space [32].

D. Preparation of liquid crystal cells

Nematic and smectic liquid crystal (5CB) cells were assembled with replicas on one surface and octadecyltriethoxysilane (OTES) SAM-coated glass slides on the other. To maintain the cell gaps, epoxy mixed with 1.2 or 7 μm silica spheres was used, respectively, for the 5CB and 8CB cells.

III. RESULTS

Figures 1(a) and 1(b) show AFM images of 200 and 400 nm square patterns on a replica. The measured depth of these

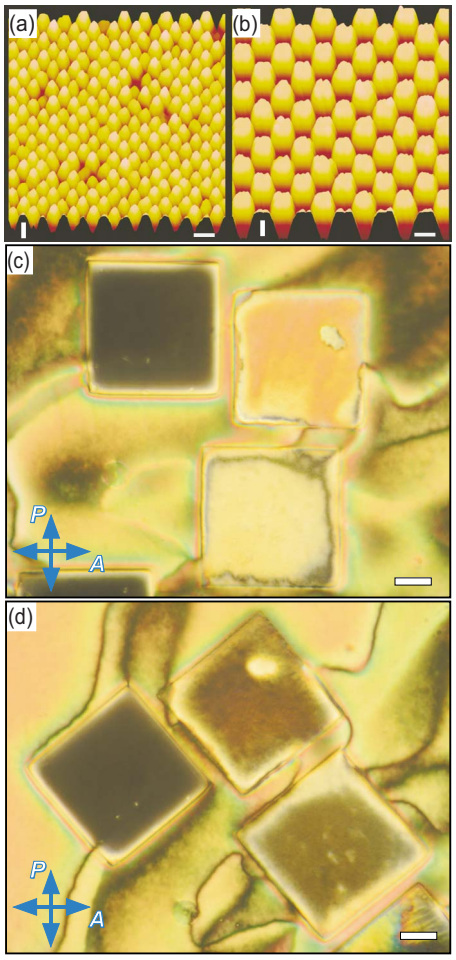

FIG. 1. (Color online) Topographically patterned alignment layers and nematic LC textures. Checkerboard patterns (a) of 200 nm squares and (b) of 400 nm squares imprinted on a polymer replica imaged using atomic force microscopy. The vertical and horizontal white scale bars in (a) and (b) represent 400 and 500 nm, respectively. (c) Depolarized transmission light microscopy image of a hybrid nematic (5CB) cell with checkerboard patterns of different square sizes (200, 600, and 400 nm from top to bottom) on one surface and an OTES SAM-coated glass slide as the other. The (pink) 600 nm patterned region has the highest birefringence, and the director is approximately planar. (d) The same sample rotated counterclockwise by 45°. The 200 nm patterned area remains dark, confirming that the director orientation there is homeotropic. The gap between the two surfaces was established by 1.2 μm silicon beads. The scale bars in (c) and (d) represent 20 μm.

wells is about 400 and 600 nm, respectively, a difference that may reflect inefficient etching or be an artifact caused by the inability of the AFM tip to access the bottoms of these narrow wells. The buttes on the replica are higher at their centers, probably due to the shape of the mold: after reactive ion etching, it is expected that the centers of the wells in the mold would be somewhat deeper than the edges. The patterning is uniform in each 80 μm square area.

Since liquid crystals are birefringent, the director field can be determined unambiguously by observing the LC cell between crossed polarizers, the optical transmission of the cell depending on the director orientation relative to the polarizers. Figures 1(c) and 1(d) show depolarized transmission light microscopy images of the nematic liquid crystal (5CB) cell. The director is homeotropic at the SAM and planar at the polymer surface everywhere it is not patterned. In Fig. 1(c), the upper left region, which is patterned with the 200 nm squares, is dark while the two other regions, patterned with 600 and 400 nm squares, are brighter. When the cell is rotated, as shown in Fig. 1(d), the 200 nm checkerboard area remains dark, confirming that this region is essentially homeotropic. The other two patterned regions in Fig. 1(d) are partially extinguishing, with the average director field of the coarser checkerboards pretilted along a diagonal direction (at $\pm 45°$ to the squares), similar to the planar bistable orientations seen in earlier experiments [9]. As the periodicity of the checkerboards increases, the degree of homeotropic alignment becomes weaker and the degree of ordering decreases near the boundaries of the patterned regions, as observed previously in related systems [30]. It is clear that the alignment is being determined by the patterned thiol-ene surface rather than by the homeotropic SAM, since the regions that are not patterned show significant birefringence and no indication of homeotropic alignment. Even assuming the SAM imposes perfect homeotropic anchoring, the critical thickness ($d_c = K/\gamma$) for the transition from a hybrid state to a uniform homeotropic configuration is calculated to be only 78 nm, which is much smaller than the thickness of our cells [33].

Homeotropic alignment is also observed in the area of the smectic liquid crystal (8CB) cell patterned with 200 nm wells, as shown in Fig. 2. Homeotropic (dark) regions occur even in the 400 and 600 nm patterned regions of this cell, in coexistence with planar (focal conic) domains, although the planar orientation clearly becomes more dominant as the wells get wider. The boundaries of the patterned regions are much sharper in the smectic case than in the nematic because bend and twist distortions of the director are forbidden in smectics [34,35].

We reported previously that the director in nematic cells, where the alignment layer is patterned with wide shallow wells, orients parallel to the glass substrates [9,30]; the LC is also aligned parallel to the inner faces of each well, leading to a bistable distorted planar state with the average director orientation along a diagonal of the square similar to the configuration shown in the inset of Fig. 3. The transition to homeotropic orientation when the wells are narrow and deep can be understood as follows: as the width of a hypothetical well of fixed depth with planar alignment is reduced, the spatial gradients of the director field increase. The Frank elastic energy density (which is proportional to the square of these gradients) increases correspondingly until it exceeds the planar anchoring energy of the polymer film, at which point the bottom of the well goes homeotropic and this also becomes the preferred director orientation in the cell. According to this picture, homeotropic alignment should be preferred in narrow deep wells.

IV. THEORY

To calculate the elastic energy of the LC in the topographically patterned regions, we assume that the surface

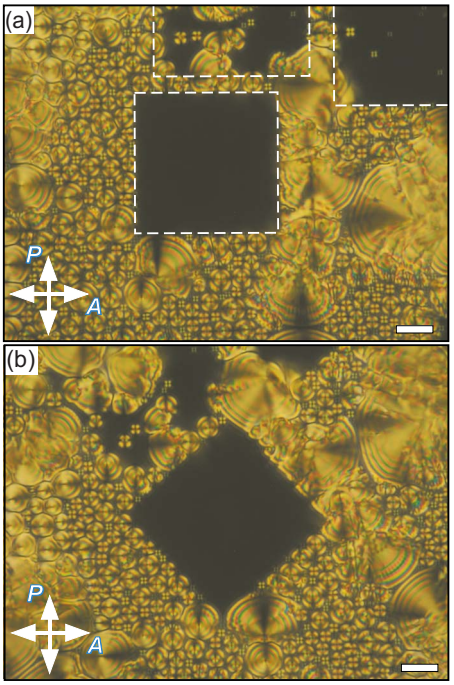

FIG. 2. (Color online) Topographic alignment of smectic-*A* liquid crystal. (a) Depolarized transmission light microscopy image of a smectic (8CB) cell with checkerboard patterns of different square sizes on one surface and an OTES SAM-coated glass slide for the other surface. The gap between the two surfaces was maintained by 7 μm silicon beads. The center pattern has 200 nm squares, with 600 and 400 nm square patterns at the top middle and top-right corner, respectively. The boundaries of the patterned regions (indicated by dashed lines) are sharper than in the nematic cell in Fig. 1. The larger scale patterns show homeotropic regions coexisting with the planar (focal conic) texture favored in the non-patterned areas of the replica. (b) The same sample rotated counterclockwise by 45°. The white scale bars represent 20 μm.

comprises an array of idealized square wells with flat tops. As long as the director in the well remains in the plane of the surface, the director field $\phi(x,y)$ is two dimensional and satisfies Laplace's equation in the one-elastic constant limit. The director field in the well can be determined exactly in this model using conformal mapping techniques described in detail in the Appendix. The elastic energy in a well of width L is then found to be

$$F = \pi Kh\left[\ln\left(\frac{L}{\delta}\right) - 0.617\ 386\cdots\right],$$

where K is the Frank elastic constant, δ is the radius of topological defects in the corners of the well, and h is the well depth. A similar result has been found for nematics confined to cylindrical pores [36,37]. The free-energy density of an array of such square wells when $h=400$ nm is plotted in Fig. 3. The dependence on well width was computed by multiplying the number of wells per unit area by the elastic energy of a single well, assuming the director field varies in two dimensions only as depicted in the inset. The energy of each of the defects [shown as vertical (red) lines in the inset] was taken to be $F_{\text{defect}}=\pi Kh/4$ [38]. Taking the average elastic constant of 5CB as $K=7.2$ pN [39], this theory predicts that when the wells are less than $L\approx 456$ nm wide, the elastic energy density of the distorted planar state of the 5CB/thiol-ene system exceeds the surface energy anisotropy and the homeotropic state is favored.

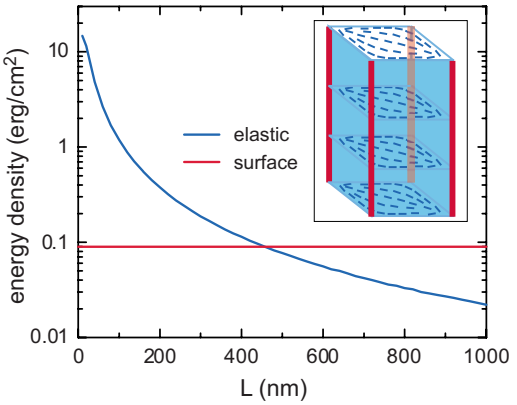

FIG. 3. (Color online) Comparison of LC surface anchoring and elastic energies with well size. The curve (blue) shows the elastic energy density of LC in a distorted planar configuration (see inset) on checkerboard patterns as a function of well width L. The horizontal line (red) represents the surface polar anchoring energy, i.e., the energy density of homeotropically oriented LC. The thick vertical lines drawn along the edges of the well represent defects in the director field. These defects terminate at the tops of the wells, with the director field in the bulk LC above varying continuously in space.

V. NUMERICAL SIMULATION

In highly frustrated nematics, where local biaxiality and gradients in the order become important, the free energy cannot be described satisfactorily using a Frank elastic model based on a scalar order parameter S and the director **n**. In this case, a full tensorial representation, using a tensor order parameter $\boldsymbol{Q}$, is required to correctly describe the nematic structure [40,41]. We have computed the director configuration in LC cells topographically patterned with channels [or two-dimensional (2D) wells] $h=400$ nm deep with widths in the range $200<L<800$ nm using a finite-element implementation of a tensorial nematic description [42]. We find that the director field in each well adopts a hybrid configuration in this model, with the director orientation changing from planar to homeotropic as we move away from the bottom center of the well [43].

The nematic texture that minimizes the thermodynamic free energy F of the system may be found using a tensorial description, in which the nematic phase is fully described by a tensor order parameter $\boldsymbol{Q}$, and the nematic distortions are expressed by spatial variations in the eigenvectors and eigenvalues of $\boldsymbol{Q}$. In general, $\boldsymbol{Q}$ is a symmetric, traceless tensor of second rank, $\boldsymbol{Q}=S_1(\boldsymbol{n}\otimes\boldsymbol{n}-\frac{1}{3}\boldsymbol{I})+S_2(\boldsymbol{m}\otimes\boldsymbol{m}-\frac{1}{3}\boldsymbol{I})$, where S_1 and S_2 are scalar order parameters, and $\boldsymbol{n}$, $\boldsymbol{m}$, and $\boldsymbol{n}\times\boldsymbol{m}$ are the eigenvectors of $\boldsymbol{Q}$, with the corresponding eigenvalues $(2S_1-S_2)/3$, $(2S_2-S_1)/3$, and $-(S_1+S_2)/3$ [44]. In the case of uniaxial order, two of these eigenvalues are equal, so S_1

$=0$, $S_2=0$, or $S_1=S_2$, and the largest eigenvalue is $2S/3$, where S is S_1 or S_2. In the biaxial states, the three eigenvalues are all different, with the maximum biaxiality arising when one eigenvalue is zero. This description enables the analysis of textures of highly frustrated calamitic nematic materials by taking into account local biaxial configurations, as in the case of the core of a defect [45] or of order reconstruction phenomena [46]. Moreover, the $\boldsymbol{Q}$ tensor model can describe the effect of an isotropic surface on the nematic molecules, for instance a surface giving planar degenerate anchoring (with the nematic director constrained to be parallel to the surface) but where the nematic order is biaxial [47].

We define a Landau–de Gennes free-energy functional,

$$\boldsymbol{F}(\boldsymbol{Q},\partial\boldsymbol{Q}) = \boldsymbol{F}_d(\boldsymbol{Q},\partial\boldsymbol{Q}) + \boldsymbol{F}_t(\boldsymbol{Q}) + \boldsymbol{F}_s(\boldsymbol{Q}) = \int_\Omega [f_d(\boldsymbol{Q},\partial\boldsymbol{Q}) + f_t(\boldsymbol{Q})]\, d\Omega + \int_\Gamma f_s(\boldsymbol{Q})\, d\Gamma.$$

The terms $f_d(\boldsymbol{Q},\partial\boldsymbol{Q})$ and $f_t(\boldsymbol{Q})$ are the volumetric free-energy densities due to the elastic and thermotropic contributions, and the term $f_s(\boldsymbol{Q})$ is the surface free-energy density due to the interaction of the nematic material with the bounding surfaces. The thermotropic free-energy density is typically a truncated expansion in the scalar invariants of the tensor $\boldsymbol{Q}$,

$$f_t(\boldsymbol{Q}) = a\ \mathrm{tr}\,(\boldsymbol{Q}^2) - \frac{2b}{3}\mathrm{tr}\,(\boldsymbol{Q}^3) + \frac{c}{2}(\mathrm{tr}\,(\boldsymbol{Q}^2))^2.$$

The coefficients a, b, and c are in general temperature dependent, but it is usual to approximate this dependency by assuming that b and c are independent of temperature while $a=\alpha(T-T^*)=\alpha\,\Delta T$, where $\alpha>0$ and T^* is the temperature at which the isotropic phase becomes unstable. At each temperature T, this term forces the calamitic nematic phase to assume an equilibrium state with a scalar order parameter S_{eq} that minimizes $f_t(\boldsymbol{Q})$ given by

$$S_{\mathrm{eq}}(\Delta T) = \frac{b}{4c}\left(1 + \sqrt{1 - \frac{24\,ac}{b^2}}\right).$$

The elastic density energy $f_d(\boldsymbol{Q},\partial\boldsymbol{Q})$ penalizes any deviation from a spatially homogeneous texture of $\boldsymbol{Q}$, any gradient of $\boldsymbol{Q}$, leading to an increase in the distortion energy. Specifically,

$$f_d(\boldsymbol{Q},\partial\boldsymbol{Q}) = \frac{L_1}{2}(Q_{ij,k})^2 + \frac{L_2}{2}Q_{ij,j}\,Q_{ik,k} + \frac{L_6}{2}Q_{lk}\,Q_{ij,l}\,Q_{ij,k},$$

where $Q_{ij,k}$ is the spatial derivate of the ijth element of $\boldsymbol{Q}$ with respect to the x_k geometric coordinate, and L_1, L_2, and L_6 are related to the Frank elastic constants K_1, K_2, and K_3 by

$$L_1 = \frac{1}{6S_{\mathrm{eq}}^2}(K_3 - K_1 + 3K_2),$$

$$L_2 = \frac{1}{S_{\mathrm{eq}}^2}(K_1 - K_2),$$

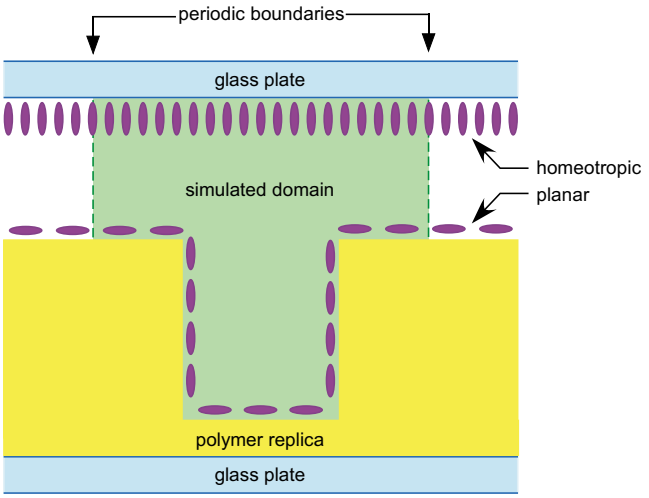

FIG. 4. (Color online) Simulation geometry. The director orientation is computed in a cross section of a liquid crystal cell where one substrate is a polymer replica topographically patterned with an array of square wells, approximated here by infinitely long channels. Planar degenerate anchoring is assumed on the replica, with the upper surface being homeotropic. The simulated domain (shown in green) extends half way to the next channel in each direction, allowing the use of periodic boundary conditions

$$L_6 = \frac{1}{2S_{\mathrm{eq}}^3}(K_3 - K_1).$$

As the thiol-ene polymer gives rise to planar degenerate anchoring of nematic molecules on the replica, we may express $f_s(\boldsymbol{Q})$ as $f_s=(W/2S_s)\boldsymbol{\upsilon}\cdot\boldsymbol{Q}\cdot\boldsymbol{\upsilon}$, where $\boldsymbol{\upsilon}$ is the local normal to the boundary surface, i.e., nematic molecules align parallel to the polymer substrate without any preferred azimuthal direction [47,48]. In accord with the experimental measurements, we take $W=9\times10^{-5}$ J m^{-2}. The surface scalar order parameter S_s is assumed to be equal to the bulk scalar order parameter with a value of 0.5 at $\Delta T=-2°$. We model the director configuration in a unit cross section of a LC cell with a large array of square wells on one substrate by computing the director field across a single infinitely long channel and applying periodic boundary conditions at the lateral edges of the numerical domain. The anchoring on the upper boundary is set to be homeotropic. The simulation geometry is sketched in Fig. 4.

We express $\boldsymbol{Q}$ as five independent components $\boldsymbol{q}_1$, $\boldsymbol{q}_2$, $\boldsymbol{q}_3$, $\boldsymbol{q}_4$, and $\boldsymbol{q}_5$ for computational convenience and use a finite-element method to find the ground configuration of $F(\boldsymbol{Q},\partial\boldsymbol{Q})$, corresponding to solving the following five coupled nonlinear partial differential equations:

$$\sum_{j=1}^{2}\frac{\partial}{\partial x_j}\left(\frac{\partial f_b}{\partial q_{i,j}}\right) = \frac{\partial f_b}{\partial q_i} \quad \text{for} \quad i = 1\cdots5$$

$$\text{where} \quad q_{i,j} = \partial q_i/\partial x_j \quad \text{and}$$

$$f_b = f_d(\boldsymbol{Q},\partial\boldsymbol{Q}) + f_t(\boldsymbol{Q}).$$

Even though we solve only a stationary problem, we have for convenience introduced a time derivative to apply iterations

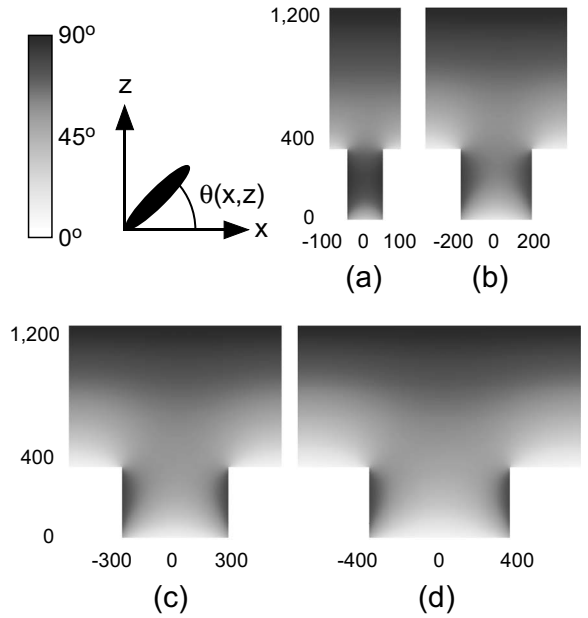

FIG. 5. Simulated director tilt angle $\theta(x,z)$ for cross section of LC cells. The cell has homeotropic anchoring on the top surface and the bottom patterned with long rectangular channels of depth $h=400$ nm and different widths L: (a) 200, (b) 400, (c) 600, and (d) 800 nm. In narrow channels, the orientation of the director is predominantly homeotropic, while in wider channels the texture gradually evolves toward a quasiplanar (hybrid) configuration, similar to the behavior observed experimentally with square wells. The equivalent cell thickness is $t=1.2$ μm. The shading shows the local director orientation: white is horizontal and black is vertical. The simulations were performed using the material coefficients of 5CB at temperature $\Delta T=T-T^*=-2.0$ °C: $K_1=4.1\times10^{-12}$ N, $K_2=2.7\times10^{-12}$ N, and $K_3=5.0\times10^{-12}$ N. The thermodynamic coefficients of the Landau–de Gennes expansion described in text were taken to be $\alpha=0.13\times10^6$ J/(Km^3), $b=1.6\times10^6$ J/m^3, $c=3.9\times10^6$J/m^3, and $a=\alpha\Delta T=2.6\times10^5$ J/m^3, giving a scalar order parameter $S_{eq}=0.345$.

until a stable steady-state solution is obtained, discretizing in time via a semi-implicit Euler method [46]. This time-dependent equation is derived by balancing the dissipative energy and free-energy variations, where the dissipation results from director motion and changes in the nematic order rather than from viscous flow [49].

Model results for the 5CB/thiol-ene system, summarized in Fig. 5, show a trend that is in accord with the experimental observations. The simulations suggest that there should be a continuous transition from a quasihomeotropic state when the well width is small ($L=200$ nm) [Fig. 5(a)] to a quasiplanar (hybrid) configuration when the wells are wider ($L=800$ nm) [Fig. 5(d)]. The numerical calculations do not produce defects along the lower corners of the channels due to the low anchoring strength of the polymer films. Such defects would form only if the anchoring strength were higher.

VI. CONCLUSION

Topographic-pattern-induced vertical (homeotropic) alignment of rod-shaped liquid crystals in both nematic and smectic phases has been achieved using deep nanoscale arrays of square wells prepared by nanoimprinting a polymer alignment layer that prefers horizontal (planar) alignment in the absence of patterning. When the wells are further apart, we obtain tilted alignment with nematics and coexistence of planar and homeotropic domains with smectics. Homeotropic alignment of the nematic phase is predicted theoretically by comparing the surface anchoring energy of the polymer with the elastic energy density induced by the patterns, as well as by computer simulations of the director field in 2D square channels. The discovery that nanoimprinting can be used to achieve planar, tilted, or homeotropic alignment on the same surface suggests that this is a promising approach for aligning complex LCs at low cost and, more generally, that topographic patterning could be a versatile tool for allowing custom alignment of anisotropic soft matter such as block copolymers and organic semiconductors in order to optimize their performance in novel devices [50,51]. The application of the nanoimprint alignment of LCs to real devices will become more viable as nanoimprint lithography and mold fabrication techniques advance.

ACKNOWLEDGMENTS

We are grateful to our colleagues Chris Bowman and Vaibhav Khire for providing the thiol-ene material used in these experiments. This work was supported by NSF MRSEC under Grant No. DMR-0213918 and by the Italian CNR project LiCryLMD under Grant No. P10.009.

APPENDIX: ELASTIC ENERGY OF NEMATIC LIQUID CRYSTAL CONFINED TO A SQUARE WELL

This appendix derives the elastic energy of the equilibrium nematic director field in a shallow square well of side L and depth h, assuming planar anchoring at the boundaries and a single Frank elastic constant K. Since the director field $\phi(x,y)$ satisfies Laplace's equation in this limit, this problem is equivalent to finding the two-dimensional electrostatic energy of a square well of side L, with potentials $\pm V_0$ applied to alternating sides of the square. The electric potential $V(x,y)$ in the well corresponds to the director field $\phi(x,y)$. By symmetry, the diagonals of the square will be at zero potential so the square can be subdivided into four equivalent 45° right triangles with hypotenuse of length L and short sides of length $L/\sqrt{2}$. Figure 6 shows the placement of such a triangle in the $z=x+iy$ plane, with one of the acute angles placed at the origin and the long side, at potential V_0, lying along the positive x axis. The left half of the triangle is, by symmetry, equivalent upon reflection to the right half so the total electrostatic energy is eight times the energy within the left half of the triangle. The origin $x+iy=0$ is at the intersection of a side of zero potential and a side of potential V_0 so that the potential is singular at this point. Consequently it is necessary to exclude a small region near the corner, of radius δ, from the integration, with the result that the total energy depends logarithmically on δ—the radius of defects in the nematic director field.

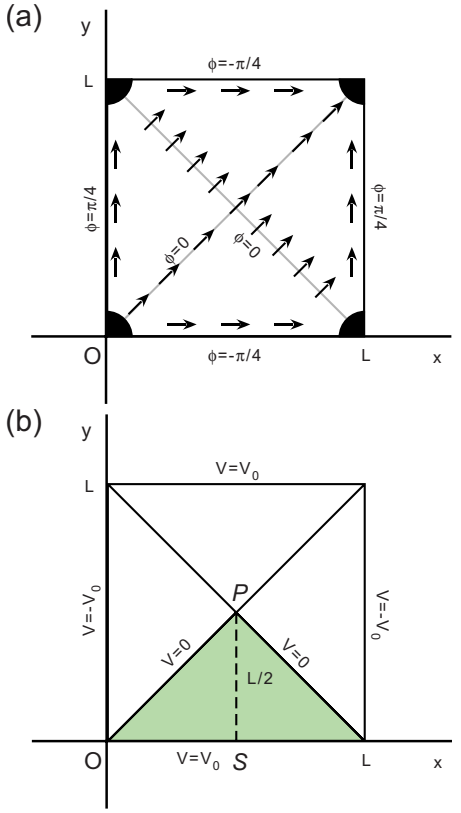

FIG. 6. (Color online) Equivalent two-dimensional liquid crystal and electrostatic problems. (a) The liquid crystal is confined to a square region of width L, with planar anchoring at the boundaries such that the average director orientation in this region is $\phi=0$. The director orientation is not defined within defects of radius δ at each corner. (b) The corresponding electrostatic problem considers the potential in a square region bounded by plates at fixed potentials $V=\pm V_0$. One fourth of the square (shown in green) consists of a 45° right triangle with its vertex at the center of the square at point P.

A Schwarz-Christoffel transformation is used here to map the interior of this triangle into the upper half of the $w=u+iv$ plane [52]. Solution of Laplace's equation in this upper half plane with boundary conditions,

$$V = V_0, \quad v = 0, \quad 0 < u < +\infty,$$

$$V = 0, \quad v = 0, \quad -\infty < u < 0, \tag{A1}$$

followed by mapping the solution back into the square in the $z=x+iy$ plane, gives the desired solution to the potential problem.

The Schwarz-Christoffel transformation for this geometry is expressed in differential form as

$$dz = dx + i\,dy = \frac{\lambda L^{5/4} dw}{(w+L)^{1/2} w^{3/4}} = (A+iB)(du+idv). \tag{A2}$$

The factor $L^{5/4}$ is inserted so that all the variables have units of length. The coefficient λ will be determined so that the triangle has the correct size. Figure 7 shows the result of the mapping in the w plane.

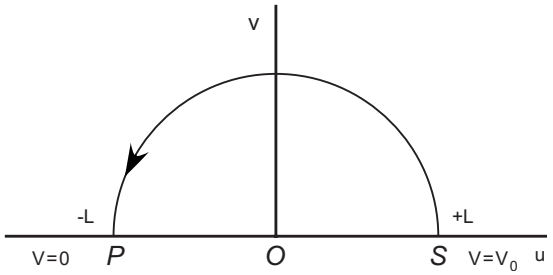

FIG. 7. The interior of the triangle (green) of Fig. 6(b) is mapped into the entire upper half of the w plane. The electric field lines are circles, with the vertical line from S to P in Fig. 6 becoming a circle of radius L. The equipotentials are radial lines at a constant angle relative to the u axis from the origin to infinity.

The energy is an area integral with area element $dxdy$. To relate this element to an area in the w plane, we first separate Eq. (A2) into its real and imaginary parts,

$$dx = A\,du - B\,dv, \quad dy = B\,du + A\,dv. \tag{A3}$$

The Jacobian of the transformation then gives

$$dx\,dy = (A^2 + B^2) du\,dv. \tag{A4}$$

In the w plane the potential that satisfies the boundary conditions is constructed as a linear function of the complex logarithm,

$$V(u,v) = V_0\,\mathrm{Im}[i - (\ln w)/\pi]. \tag{A5}$$

Thus

$$\frac{\partial V}{\partial u} = \frac{V_0}{\pi}\frac{v}{u^2+v^2}, \quad \frac{\partial V}{\partial v} = -\frac{V_0}{\pi}\frac{u}{u^2+v^2}. \tag{A6}$$

To obtain gradients of the potential in the z plane, we invert Eq. (A2),

$$du + idv = \frac{dx+idy}{A+iB} = \frac{Adx + Bdy + i(-Bdx + Ady)}{A^2+B^2}. \tag{A7}$$

Separating this into real and imaginary parts, we obtain

$$\frac{\partial u}{\partial x} = \frac{\partial v}{\partial y} = \frac{A}{A^2+B^2},$$

$$\frac{\partial u}{\partial y} = \frac{\partial v}{\partial x} = -\frac{B}{A^2+B^2}. \tag{A8}$$

Thus in the z plane the electric field components are

$$E_x = -\frac{\partial V}{\partial x} = -\frac{V_0}{\pi}\frac{(Av+Bu)}{(u^2+v^2)(A^2+B^2)},$$

$$E_y = -\frac{\partial V}{\partial y} = -\frac{V_0}{\pi}\frac{(Bv-Au)}{(u^2+v^2)(A^2+B^2)}. \tag{A9}$$

Figure 8 shows the equipotentials and electric field in a quarter of the square; the equipotentials radiate outward from the

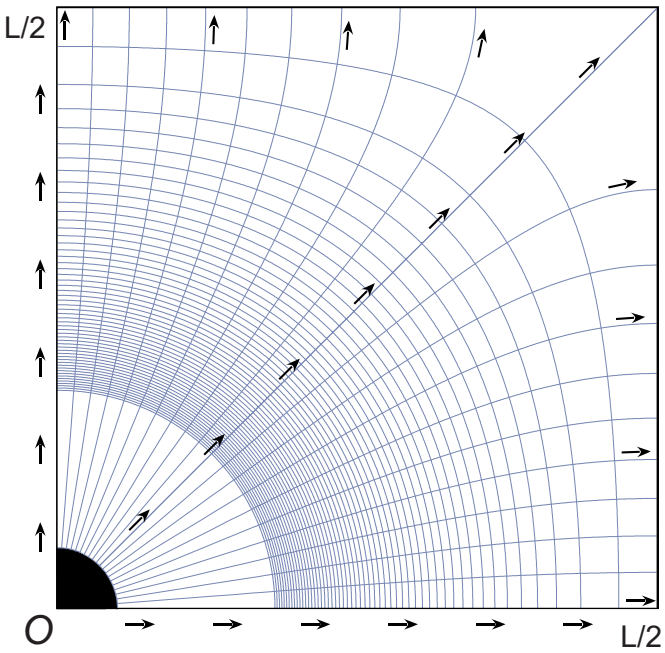

FIG. 8. (Color online) Electric field lines and equipotentials in the interior of one quadrant of the square. The equivalent nematic director orientation is along the equipotentials, as indicated schematically by the arrows. A region at the corner with circular boundary of radius δ has been excluded. The figure shows the case $\delta=0.05L$.

defect at the corner, while the electric field lines start on a side at high potential and end at a side at low potential.

The electrostatic energy density is

$$f=\frac{E_x^2+E_y^2}{8\pi}=\frac{V_0^2}{8\pi^3}\frac{1}{(u^2+v^2)(A^2+B^2)}. \tag{A10}$$

We compute the total energy by integrating the energy density over the square, assuming the director field is uniform from top to bottom of the well—this gives a factor h. Then we integrate over the interior of the triangle and transform it into an integral over the corresponding region in the w plane with the help of Eq. (A4),

$$F=h\int f(A^2+B^2)du\,dv=\frac{hV_0^2}{8\pi^3}\int\frac{du\,dv}{u^2+v^2}. \tag{A11}$$

The factors (A^2+B^2) cancel. The interior of the half circle of radius L in the w plane maps into the triangle OSP of Fig. 6. The integral is taken over the interior of the circle of radius L in the w plane. Passing to polar coordinates $\{R,\Theta\}$ in the w plane and inserting the factor 8, the energy will be

$$F=\frac{hV_0^2}{\pi^3}\int_{R=\Delta}^{R=L}\frac{RdR}{R^2}\int_{\Theta=0}^{\Theta=\pi}d\Theta=\frac{hV_0^2}{\pi^2}\ln\frac{L}{\Delta}, \tag{A12}$$

where Δ is the lower limit on the radius R in the w plane. The lower limit δ in the z plane is quite different from Δ. Near the origin of the w plane, in the denominator of the Schwarz-Christoffel transformation we can approximate one of the factors by assuming that the size of the bite out of the corner of the triangle in the z plane is small compared to L, $(w+L)^{-1/2}\approx L^{-1/2}$. The mapping function is then approximately

$$z=\lambda L^{3/4}\int\frac{dw}{w^{3/4}}=4\lambda L^{3/4}w^{1/4}. \tag{A13}$$

The relationship between the defect radii (δ in the z plane and Δ in the w plane) is thus

$$\delta=4\lambda L^{3/4}\Delta^{1/4}\quad\text{or}\quad\Delta=\left(\frac{\delta}{4\lambda}\right)^4\frac{1}{L^3}. \tag{A14}$$

Inserting this into Eq. (A12), the energy becomes

$$F=\frac{hV_0^2}{\pi^2}\ln\left(4\lambda\frac{L}{\delta}\right)^4=\frac{4hV_0^2}{\pi^2}\left[\ln\left(\frac{L}{\delta}\right)+\ln(4\lambda)\right]. \tag{A15}$$

To determine the constant λ, imagine integrating in the w plane from the origin to $-L$ along the negative real axis. The corresponding path in the z plane should be along the 45° line from the origin to the upper corner of the triangle. Setting, $w=e^{i\pi}R$, and then letting $R=tL$, the integral is

$$\begin{aligned}\frac{L}{2}+i\frac{L}{2}&=\lambda L^{5/4}e^{i\pi/4}\int_0^L\frac{dR}{(e^{i\pi}R+L)^{1/2}(e^{i\pi}R)^{3/4}}\\&=\lambda\left(\frac{L}{\sqrt{2}}+i\frac{L}{\sqrt{2}}\right)\int_0^1\frac{dt}{t^{3/4}(1-t)^{1/2}}\\&=\lambda\left(\frac{L}{\sqrt{2}}+i\frac{L}{\sqrt{2}}\right)\frac{\sqrt{\pi}\,\Gamma(1/4)}{\Gamma(3/4)}.\end{aligned} \tag{A16}$$

This can be solved for λ,

$$\lambda=\frac{\Gamma(3/4)}{\sqrt{2\pi}\Gamma(1/4)}. \tag{A17}$$

Inserting this into Eq. (A15) gives the total electrostatic energy,

$$\begin{aligned}F&=\frac{hV_0^2}{\pi^2}\ln\left(\frac{4KL}{\delta}\right)^4\\&=\frac{4hV_0^2}{\pi^2}\left[\ln\left(\frac{L}{\delta}\right)+\ln\left(\frac{4\Gamma(3/4)}{\sqrt{2\pi}\Gamma(1/4)}\right)\right]\\&=\frac{4hV_0^2}{\pi^2}\left[\ln\left(\frac{L}{\delta}\right)-0.617\,386\cdots\right].\end{aligned} \tag{A18}$$

In the liquid crystal, the boundary potential V_0 corresponds to the director orientation $\phi_0=\pi/4$ and the elastic free-energy density may be written as $K(\nabla\phi)^2/2$, where K is the Frank elastic constant. Compensating for the prefactors introduced in Eq. (A10), we make the replacement $V_0\to\pi/4$ and multiply by $4\pi K$, giving the total elastic energy

$$F=\pi Kh\left[\ln\left(\frac{L}{\delta}\right)-0.617\,386\cdots\right]. \tag{A19}$$

[1] M. O'Neill and S. Kelly, Adv. Mater. (Weinheim, Ger.) **15**, 1135 (2003).

[2] B. Kippelen, S. Yoo, J. A. Haddock, B. Domercq, S. Barlow, B. Minch, W. Xia, S. R. Marder, and N. R. Armstrong, in *Organic Photovoltaics: Mechanism, Materials, and Devices*, edited by S.-S. Sun and N. S. Sariciftci (Taylor & Francis, Boca Raton, FL, 2005), Chap. 11.

[3] J.-H. Kim, M. Yoneya, and H. Yokoyama, Nature (London) **420**, 159 (2002).

[4] L. Schmidt-Mende, A. Fechtenkötter, K. Müllen, E. Moons, R. H. Friend, and J. D. MacKenzie, Science **293**, 1119 (2001).

[5] F. Closs, K. Siemensmeyer, Th. Frey, and D. Funhoff, Liq. Cryst. **14**, 629 (1993).

[6] D. W. Berreman, Phys. Rev. Lett. **28**, 1683 (1972).

[7] J. Fukuda, M. Yoneya, and H. Yokoyama, Phys. Rev. Lett. **98**, 187803 (2007).

[8] C. Tsakonas, A. J. Davidson, C. V. Brown, and N. J. Mottram, Appl. Phys. Lett. **90**, 111913 (2007).

[9] Y. Yi, M. Nakata, A. R. Martin, and N. A. Clark, Appl. Phys. Lett. **90**, 163510 (2007).

[10] H. Kim, J. Jung, Y. Lee, and J. Kim, Appl. Phys. Lett. **88**, 113504 (2006).

[11] R. Lin and J. A. Rogers, Nano Lett. **7**, 1613 (2007).

[12] A. S. P. Chang, K. J. Morton, H. Tan, P. Murphy, W. Wu, and S. Y. Chou, IEEE Photonics Technol. Lett. **19**, 1457 (2007).

[13] J. S. Gwag, J.-H. Kim, M. Yoneya, and H. Yokoyama, Appl. Phys. Lett. **92**, 153110 (2008).

[14] B. Zhang, F. K. Lee, O. K. C. Tsui, and P. Sheng, Phys. Rev. Lett. **91**, 215501 (2003).

[15] S. Kitson and A. Geisow, Appl. Phys. Lett. **80**, 3635 (2002).

[16] Y. J. Lim, E. Jeong, M. H. Chin, S. Ji, G. D. Lee, and S. H. Lee, J. Phys. D **41**, 085110 (2008).

[17] G. P. Bryan-Brown, C. V. Brown, and J. C. Jones, U.S. Patent No. 6,249,332 (2001).

[18] K. Ichimura, Y. Suzuki, T. Seki, and K. Aoki, Langmuir **4**, 1214 (1988).

[19] X. Lu, F. K. Lee, P. Sheng, H. S. Kwok, V. Chigrinov, and O. Tsui, Appl. Phys. Lett. **88**, 243508 (2006).

[20] V. Gupta and N. Abbott, Science **276**, 1533 (1997).

[21] J. P. Bramble, S. D. Evans, J. R. Henderson, C. Anquetil, D. J. Cleaver, and N. J. Smith, Liq. Cryst. **34**, 1059 (2007).

[22] J. Haisma, M. Verheijen, K. van den Heuvel, and J. van den Berg, J. Vac. Sci. Technol. B **14**, 4124 (1996).

[23] S. Y. Chou, P. R. Crauss, and P. J. Renstrom, Appl. Phys. Lett. **67**, 3114 (1995).

[24] E. A. Dobisz, Z. Bandic, T.-W. Wu, and T. Albrecht, Proc. IEEE **96**, 1836 (2008).

[25] F. J. Kahn, G. N. Taylor, and H. Schonhorn, Proc. IEEE **61**, 823 (1973).

[26] H. Yoshida, T. Seino, and Y. Koike, Jpn. J. Appl. Phys., Part 1 **36**, L1449 (1997).

[27] B. Park, K.-J. Han, Y. Jung, H.-H. Choi, H.-K. Hwang, S. Lee, S.-H. Jang, and H. Takezoe, J. Appl. Phys. **86**, 1854 (1999).

[28] S. C. Jain, V. K. Tanwar, and V. Dixit, Jpn. J. Appl. Phys., Part 1 **41**, L1106 (2002).

[29] S. Lazarouk, A. Muravski, D. Sasinovich, V. Chigrinov, and H. S. Kwok, Jpn. J. Appl. Phys., Part 1 **46**, 6889 (2007).

[30] Y. Yi, V. Khire, C. N. Bowman, J. E. Maclennan, and N. A. Clark, J. Appl. Phys. **103**, 093518 (2008).

[31] V. S. Khire, Y. Yi, N. A. Clark, and C. N. Bowman, Adv. Mater. (Weinheim, Ger.) **20**, 3308 (2008).

[32] A. Sugimura, T. Miyamoto, M. Tsuji, and M. Kuze, Appl. Phys. Lett. **72**, 329 (1998).

[33] A. A. Sonin, *The Surface Physics of Liquid Crystals* (Gordon and Breach, Luxembourg, 1995), pp. 23–24. Although the transition from hybrid to planar orientation is treated here, the critical thickness for the transition from hybrid to homeotropic is given, by symmetry, by the same equation.

[34] P. G. de Gennes, Solid State Commun. **10**, 753 (1972).

[35] T. J. Atherton, R. Wang, and C. Rosenblatt, Phys. Rev. E **77**, 061702 (2008).

[36] The elastic energy of a square well is similar to that of a nematic in a cylinder with strong anchoring in the circularly planar-polar configuration. Assuming the splay and bend elastic constants are equal, the elastic energy in a right cylinder of radius R is given [37] by $F_c = \pi K h \ln(R/2\delta)$. The elastic energy of the square wells modeled here turns out to be about 25% larger than that of cylinders with the same base area.

[37] S. Burylov, J. Exp. Theor. Phys. **85**, 873 (1997).

[38] M. Kleman and O. D. Lavrentovich, *Soft Matter Physics: An Introduction* (Springer-Verlag, New York, 2003), Chap. 11.

[39] M. J. Bradshaw, E. P. Raynes, J. D. Bunning, and T. E. Faber, J. Phys. (Paris) **46**, 1513 (1985).

[40] R. Barberi, F. Ciuchi, M. Iovane, D. Sikharulidze, A. Sonnet, and E. Virga, Eur. Phys. J. E **13**, 61 (2004).

[41] G. Lombardo, H. Ayeb, and R. Barberi, Phys. Rev. E **77**, 051708 (2008).

[42] G. Carbone, G. Lombardo, R. Barberi, I. Musevic, and U. Tkalec, Phys. Rev. Lett. (to be published).

[43] Although the simulations were carried out for cross sections of infinitely long channels, rather than for square wells limited in extent, as in the experiments, nevertheless the overall behavior of the director field as a function of channel width is expected to be very similar to what occurs in square wells.

[44] E. Virga, *Variational Theories for Liquid Crystals* (Chapman and Hall, London, 1994).

[45] N. Schopohl and T. J. Sluckin, Phys. Rev. Lett. **59**, 2582 (1987).

[46] G. Lombardo, H. Ayeb, F. Ciuchi, M. P. De Santo, R. Barberi, R. Bartolino, E. G. Virga, and G. E. Durand, Phys. Rev. E **77**, 020702(R) (2008).

[47] J. B. Fournier and P. Galatola, Europhys. Lett. **72**, 403 (2005).

[48] C. Tsakonas, A. J. Davidson, C. V. Brown, and N. J. Mottram, Appl. Phys. Lett. **90**, 111913 (2007).

[49] A. Sonnet and E. Virga, Phys. Rev. E **64**, 031705 (2001).

[50] S. O. Kim, H. H. Solak, M. P. Stoykovich, N. J. Ferrier, J. J. de Pablo, and P. F. Nealey, Nature (London) **424**, 411 (2003).

[51] M. L. Swiggers, G. Xia, J. D. Slinker, A. A. Gorodetsky, G. G. Malliaras, R. L. Headrick, B. T. Weslowski, R. N. Shashidhar, and C. S. Dulcey, Appl. Phys. Lett. **79**, 1300 (2001).

[52] P. M. Morse and H. Feschbach, *Methods of Theoretical Physics* (McGraw-Hill, New York, 1952), pp. 445–453.